A Midlatitude Cirrus Cloud Climatology from the Facility for Atmospheric Remote Sensing. Part III: Radiative Properties

KENNETH SASSEN AND JENNIFER M. COMSTOCK*

Department of Meteorology, University of Utah, Salt Lake City, Utah

(Manuscript received 22 August 2000, in final form 5 January 2001)

ABSTRACT

In Part III of a series of papers describing the extended time high-cloud observations from the University of Utah Facility for Atmospheric Remote Sensing (FARS) supporting the First International Satellite Cloud Climatology Project (ISCCP) Regional Experiment, the visible and infrared radiative properties of cirrus clouds over Salt Lake City, Utah, are examined. Using ~860 h of combined ruby (0.694 μm) lidar and midinfrared (9.5–11.5 μm) radiometer data collected between 1992 and 1999 from visually identified cirrus clouds, the visible optical depths τ and infrared layer emittance ϵ of the varieties of midlatitude cirrus are characterized. The mean and median values for the cirrus sample are 0.75 $\pm$ 0.91 and 0.61 for τ, and 0.30 $\pm$ 0.22 and 0.25 for ϵ. Other scattering parameters studied are the visible extinction and infrared absorption coefficients, and their ratio, and the lidar backscatter-to-extinction ratio, which has a mean value of 0.041 sr^{-1}. Differences among cirrus clouds generated by general synoptic (e.g., jet stream), thunderstorm anvil, and orographic mechanisms are found, reflecting basic cloud microphysical effects. The authors draw parameterizations in terms of midcloud temperature T_m and physical cloud thickness Δz for ϵ and τ: both macrophysical variables are needed to adequately address the impact of the adiabatic process on ice cloud content, which modulates radiative transfer as a function of temperature. For the total cirrus dataset, the authors find $\epsilon = 1 - \exp[-8.5 \times 10^{-5} (T_m + 80°\text{C})\, \Delta z]$. These parameterizations, based on a uniquely comprehensive dataset, hold the potential for improving weather and climate model predictions, and satellite cloud property retrieval methods.

1. Introduction

As recognized in the design of the First International Satellite Cloud Climatology Project (ISCCP) Regional Experiment (FIRE; Cox et al. 1987), the uncertainties in characterizing from satellites the globally abundant cirrus clouds of the upper troposphere represent a major problem in comprehending the climate of the earth. Composed of decidedly nonspherical ice crystals, ethereal enough to be often semitransparent to skylight, and confined to the frigid upper troposphere, it is not surprising that they remain one of the missing links in this endeavor. As far as their impact on climate is concerned, among the fundamental radiative properties of cirrus clouds are the visible cloud optical thickness τ and the infrared layer emittance ϵ. These quantities help prescribe the interference to the transfer of radiation that cirrus clouds cause by blocking solar radiation from reaching the underlying atmosphere and surface, and intercepting the radiation of terrestrial origin from escaping to outer space. The balance between these two processes determines the net impact of cirrus clouds on the heat balance of the earth, which are certainly an important modulator of our climate (Liou 1986).

Despite significant advances in nonspherical particle scattering theory (Mischenko et al. 2000) and computing capabilities, we are ultimately limited in our weather and climate modeling attempts by imperfect knowledge of the basic cloud properties that control radiative transfer. These properties have been shown through simulations to be both macrophysical and microphysical in nature (e.g., Stephens et al. 1990; Takano and Liou 1995; Ou and Liou 1995). Since computationally intensive large-scale models must employ considerable simplifications, treatments of cirrus radiative properties tend to be based on limited aircraft observations, which ignore fundamental variations in the vertical and horizontal content of cirrus (Khvorostyanov and Sassen 1998). An alternative approach is to obtain parameterizations of cirrus radiative properties directly from comprehensive measurements in the visible and infrared portions of the spectrum.

In this third part of a series of papers providing the results of an extended time cirrus cloud observation program begun in 1986 in support of FIRE, we present

* Current affiliation: Pacific Northwest National Laboratory (operated by Battelle for the U.S. Department of Energy), Richland, Washington.

Corresponding author address: Kenneth Sassen, 135 S. 1460 E. (819 WBB), University of Utah, Salt Lake City, UT 84112.
E-mail: ksassen@met.utah.edu

a climatology of cirrus cloud radiative properties obtained using an improved combined visible lidar–infrared radiometer (LIRAD) method (Barnett 2000; Comstock and Sassen 2001). This high cloud remote sensing tool was pioneered by Platt (1973). The derived quantities include τ, ϵ, the volume extinction and absorption coefficients, the layer integrated ratio of these coefficients, and the lidar backscatter-to-extinction ratio. The measurements were collected over a 7-yr period from the University of Utah Facility for Atmospheric Remote Sensing (FARS; Sassen et al. 2001a). In Sassen and Campbell (2001, hereafter Part I) the macrophysical and synoptic properties of our variety of midlatitude cirrus clouds are described, and in Sassen and Benson (2001, hereafter Part II) the cloud microphysical properties derived from lidar depolarization data are evaluated.

2. The FARS cirrus cloud LIRAD dataset

The nature of the dataset used here differs somewhat from those used in Parts I and II because of the more limited availability of the PRT-5 type infrared radiometer (IR) data. The narrow-beam (0.14°) midinfrared (9.5–12 μm) radiometer was acquired in 1992 from Pyrometer Instrument Company, Inc., and has undergone three factory calibrations. It has a minimum effective blackbody temperature of ~ -80°C (1.84 W m^{-2} sr^{-1} radiance). Since under cloudless skies the main source of downwelling radiance comes from water vapor emissions, this limit can be exceeded under dry winter conditions: for moist summer conditions, temperatures > -30°C can be encountered. The detector has a time response of 0.3 s, but the signals are generally recorded every 10 s at the time of each lidar shot, and both are averaged over 2-min (10–12 shot) intervals in this study to improve signal quality.

The IR is mounted on the cloud polarization lidar (CPL) table and coaligned with the lidar using a bore sighted spotting scope. This ''turnkey'' lidar system is based on a high-power (1.5 J) ruby (0.694 μm) laser transmitter with a pulse length of $\sim$25 ns, a pulse rate of 10 s per shot, and a full beam divergence of 1 mrad. The 28-cm telescope receiver, normally operated at a 1 mrad field of view (FOV), contains dual analog photodetectors to measure (at 7.5-m resolution) the backscattered components in the parallel (i.e., vertical) and perpendicular planes of polarization. For the lidar data used in this study, the two signal components are combined after accounting for channel gains into a single ''unpolarized'' signal. More complete descriptions of the FARS instrumentation and data display examples can be found in Sassen (1997, 2001) and Sassen et al. (2001a).

Between 1992 and 1999, a total of $\sim$860 h of combined IR and CPL data from cirrus clouds proved suitable for the LIRAD analysis, as described in detail in Barnett (2000) and outlined below in section 3. All the data included here are from cirrus clouds that were visually identified by a trained observer. However, not all cirrus clouds studied during this period were suitable for analysis, somewhat restricting the sample. As a consequence of the relative insensitivity of the LIRAD method to subvisual or very thin cirrus, because the weak downwelling cloud signals can be negligibly small compared to the gaseous (principally water vapor) emittances, such clouds are generally lacking in this sample. Usually, under typically dry atmospheric conditions in the eastern Great Basin, a discernible IR signal is noted for lidar-derived $\tau > \sim 0.05$. On the other hand, because some optically thicker cirrus contain strongly backscattering layers that cause the signal gains to be considerably reduced due to the limited (8 bit) dynamic range of the digitizers, the location of the cloud top can be lost. Without knowledge of cloud thickness, the analysis is incomplete. Finally, multilayer cirrus clouds were not treated if the separation between the layers was $>$2.0 km. Thus the physical cloud thickness reported is essentially the same as the envelope method used in Part I.

TABLE 1. Percentage of total number of 2-min average observations that fall under each cloud generating mechanism.

Generating mechanism	Percent of total observations	Number of averages
Synoptic	60.6	15 603
Anvil	13.8	3567
Contrail	7.53	1941
Subtropical	7.45	1919
Orographic	4.23	1055
Altostratus	1.00	257
Other	0.82	211

We also introduce a new consideration into our analysis scheme. Using field notes describing the likely origin of the cirrus, the sample is stratified by the cirrus generating mechanism. Table 1 shows the division of the ice cloud dataset into the generation mechanism. It should be noted, however, that the cirrus identification may reflect a mixture of cirrus cloud types, especially for the orographic case in which advecting synoptic cirrus is orographically enhanced at relatively low altitudes, or the frequent case when contrail-generated cirrus is mixed with synoptic cirrus. Of the categories listed in Table 1, the synoptic, anvil, and orographic cirrus types appeared distinct and were treated separately. In practice, anvil cirrus combine those clouds visually associated with cumulonimbus clouds of local origin, regional origin as indicated by Utah radar or satellite information, or from general synoptic conditions favorable for the advection of the remnants of anvils generally from the southwest during monsoonal conditions (Part I). Orographic cirrus clouds typically consist of visually identified wave cloud formations from the upwind ($\sim$10 km) Oquirrh mountain range, but they are also, on occasion, evident in satellite imagery as cirrus clouds generated by mountain ranges as far away as the California

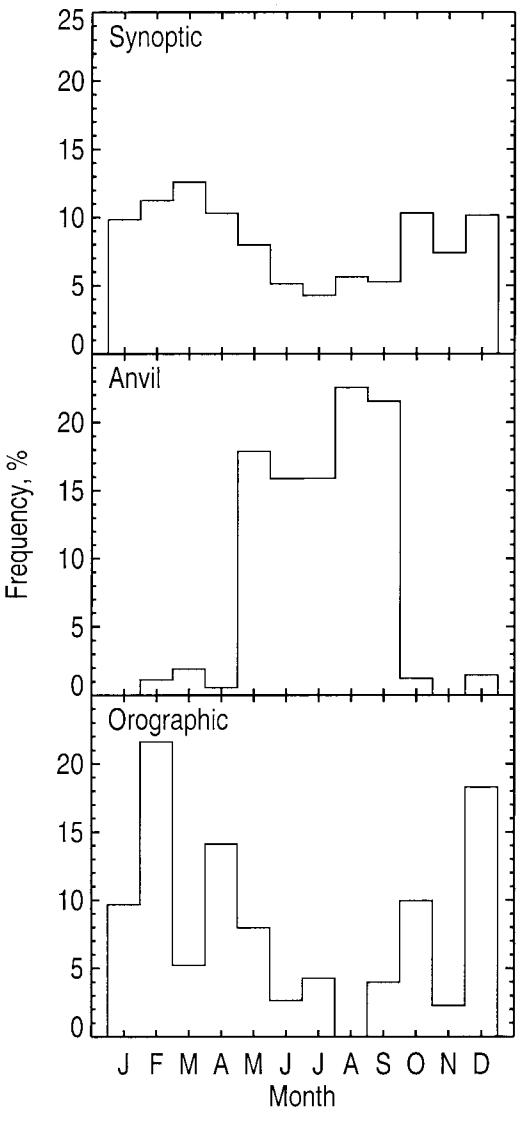

FIG. 1. The monthly frequency of occurrence of the three main cirrus categories based on cloud generating mechanism.

Sierra range, implying cirrus clouds that are in a maintenance stage. Synoptic cirrus, on the other hand, refer to the general formation and advection of midlatitude cirrus preceding weather disturbances and associated with jet streams/streaks, closed lows, etc. The total of all cirrus clouds sampled at FARS regardless of generating mechanism is referred to as our ''midlatitude'' sample.

In Fig. 1 is shown the average monthly frequencies of occurrence (in percent of the total) for these cirrus generating mechanisms. In agreement with the general synoptic weather discussions in Part I, we see a minimum in synoptic cirrus occurrence during summer when jet stream systems are generally far to the north of FARS, but anvils are most common during the summer monsoon season. Orographically generated cirrus are most frequently observed under the coldest seasonal conditions.

TABLE 2. Cloud macrophysical statistics divided into categories based on the primary cirrus generating mechanisms observed at FARS. Heights are above MSL.

	Mean	Median	Mean	Median
	Cloud-top height (km)		Cloud-top temperature (°C)	
Midlatitude	10.97 ± 1.72	11.38	−52.9 ± 11.6	−55.5
Synoptic	11.26 ± 1.42	11.53	−55.8 ± 9.3	−57.7
Anvil	10.93 ± 1.26	11.15	−47.1 ± 9.1	−48.3
Orographic	9.92 ± 1.60	10.03	−47.7 ± 10.2	−50.1
	Midcloud height (km)		Midcloud temperature (°C)	
Midlatitude	9.57 ± 1.70	9.80	−42.6 ± 11.3	−43.4
Synoptic	9.82 ± 1.51	9.95	−45.1 ± 9.8	−45.5
Anvil	9.64 ± 1.28	9.80	−37.3 ± 9.0	−37.9
Orographic	8.74 ± 1.49	8.72	−39.1 ± 10.0	−41.8
	Cloud-base height (km)		Cloud-base temperature (°C)	
Midlatitude	8.17 ± 1.95	8.38	−32.0 ± 12.6	−31.4
Synoptic	8.39 ± 1.86	8.53	−34.2 ± 11.9	−33.3
Anvil	8.35 ± 1.53	8.53	−27.5 ± 10.3	−27.2
Orographic	7.58 ± 1.61	7.62	−30.4 ± 11.2	−31.5
	Cloud thickness (km)		Optical midcloud temperature	
Midlatitude	2.79 ± 1.38	2.63	−41.7 ± 12.5	−42.5
Synoptic	2.87 ± 1.36	2.70	−44.4 ± 11.2	−45.0
Anvil	2.58 ± 1.16	2.40	−36.7 ± 10.2	−37.1
Orographic	2.32 ± 1.23	2.03	−37.9 ± 10.5	−41.0

Although in Part I we have provided comprehensive cirrus cloud macrophysical statistics, here we supplement this information with additional data in dealing with midcloud temperature T_m and the cloud generating mechanism stratifications. We provide in Table 2 the mean and median values of a number of cloud parameters as a function of cirrus cloud type. It is clear that in going from synoptic to anvil to orographic cirrus, cloud heights and thicknesses decrease and temperatures increase. Due to the characteristic skewness in the frequency distributions, the median values tend to be higher in altitude and colder in temperature. The category ''optical midcloud temperature'' refers to the temperature at the cloud level that divides τ in half. For reference, Figs. 2 and 3 show the form of the height [all heights are given above mean sea level (MSL)] and temperature probability density functions (PDFs) for the midlatitude cirrus sample.

Shown in Fig. 4 are PDFs of cloud physical thickness Δz for the total midlatitude and three major cirrus subgroups. Although each category display Δz up to ~7.0 km, a characteristic of the orographic cases is the abundance of relatively narrow (<1.5 km) layers: many of the thicker layers likely represent mixtures of advecting synoptic and lower orographic cirrus of local origin. Last, depicted in Fig. 5 is the dependence of cloud thickness on T_m for the four cirrus categories. The FARS data

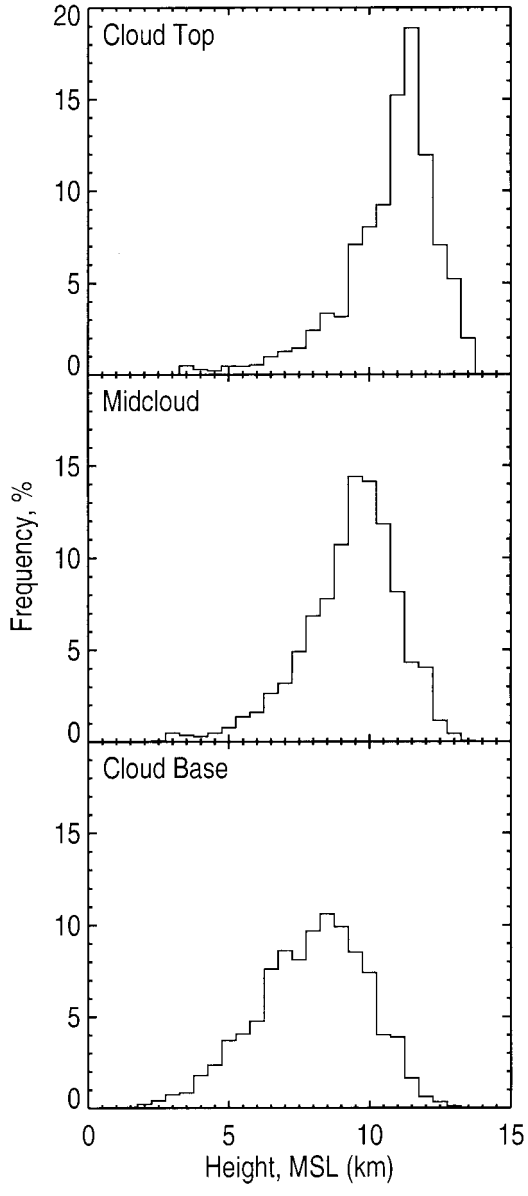

FIG. 2. PDFs of the variabilities in cloud heights for the total midlatitude cirrus cloud sample.

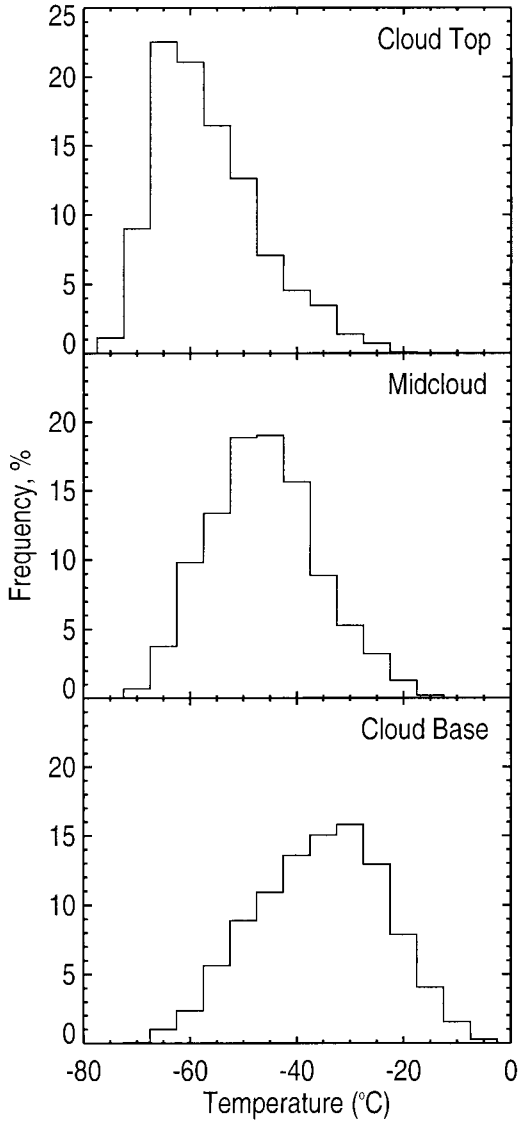

FIG. 3. PDFs of the variabilities in cloud temperatures for the total midlatitude cirrus cloud sample.

are compared with the Southern Hemisphere midlatitude cirrus reported by Platt and Dilley (1981) and findings from Minnis et al. (1990) based on FIRE intensive field observation (IFO) lidar data from Wisconsin. The total and synoptic FARS, and FIRE IFO data are in good agreement with their Australian counterpart except at warmer temperatures, where the decreasing thickness trend may be a result of sampling middle-level mixed-phase clouds (see Part II) and strongly attenuating altostratus. Reflecting the different generating mechanisms, the anvil and orographic cirrus thicknesses tend to be less dependent on T_m.

3. The LIRAD method

The retrieval algorithm used to derive cirrus radiative properties is based on the LIRAD method, which combines backscatter lidar and IR measurements with a radiative transfer model to derive ϵ and τ. The lidar profile is used to measure cloud boundaries and estimate τ, and provides a vertical distribution of backscattering that is weighted to help derive the absorption coefficient. The basic lidar equation describing the backscattered power is given by

$$P(R) = \frac{K}{R^2}[\beta(R) + \beta'(R)] \exp\left[-2\int_{R_0}^{R} \eta(R)\sigma(R)\, dR\right], \quad (1)$$

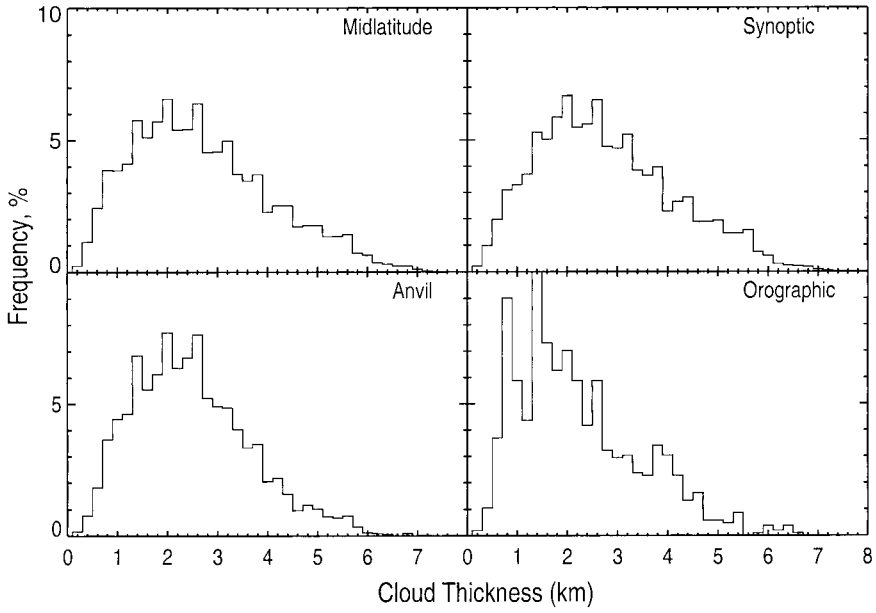

FIG. 4. PDFs of Δz for the four cirrus categories.

where K is the lidar system constant; R is the range (km); σ the volume extinction coefficient (km^{-1}); $\eta(R)$ the multiple forward-scattering correction factor; and β and β' denote the volume backscatter coefficients (km^{-1}) responsible for single and multiple scattered returned energy, respectively.

The cloud backscatter coefficient β_c required for the estimation of τ, is calculated as a function of height following the equations (Sassen and Cho 1992)

$$\beta_c(z) = \frac{G(z_0, z)}{1 - \dfrac{2\eta}{k}\displaystyle\int_{z_0}^{z} G(z_0, z')\, dz'} - \beta_m(z) \qquad (2a)$$

and

$$G(z_0, z) = \beta_m(z_0)\frac{S(z)z^2}{S(z_0)z_0^2} \times \exp\left[2\left(\frac{8\pi}{3} - \frac{\eta}{k}\right)\int_{z_0}^{z} \beta_m(z'')\, dz''\right], \qquad (2b)$$

where the scattering contribution due to air molecules β_m is removed from the total backscattered signal, and $S(z_0)z_0^2$ corresponds to the lidar signal minima, which is assumed to be due to pure molecular scattering, that occurs just below cloud base. The backscatter-to-extinction ratio k (km^{-1}; where the reciprocal is known as the lidar ratio) is equivalent to the normalized scattering phase function at 180°, or $P(\pi)/4\pi$, and is a measure of the backward strength of cloud particle scattering. This definition of k is different from that used in past LIRAD studies (Platt and Dilley 1981), where k is 4π times the normalized scattering phase function and is unitless. The η in Eq. (2) represents a correction factor to the Beer–Lambert law to account for forward multiple scattering in the lidar FOV. It is assumed to be height-independent as a simplification here, but in reality it should be expressed as $\eta(R)$ as in the attenuation term of Eq. (1). Due to the strong forward diffraction peak in ice crystal phase functions, some (up to one-half) of the scattered photons will remain indefinitely in the laser beam. This parameter does not correct for multiple backscattering stemming from other primary scattering angles, however, which must be treated by the β' term. Currently, there is no solution available describing this amount of multiple backscattering, so we have neglected β' rather than include this additional scattered component in the exponential attenuation term.

According to Mie calculations of forward multiple scattering using the model described in Sassen and Zhao (1995), η would likely have a value between 0.5 and 1.0 for the 1 mrad FOV of the CPL. The condition $\eta = 1.0$ represents the case where backscattering is due entirely to single scattering, whereas $\eta = 0.5$ corresponds to the large particle limit in which all diffracted energy remains in the lidar FOV. Results reported in Eloranta et al. (1998) using an analytical model compare well with the Mie results.

In the present study, η is chosen based on cloud observations reported in field notes and by examining height versus time displays of backscattering (Barnett 2000). Each observation period was divided into sections of various lengths based on apparent homogeneity in terms of backscattering and depolarization, and cloud depth. For example, an optically and physically thin cloud is assumed to have a value of $\eta = 0.9$ because

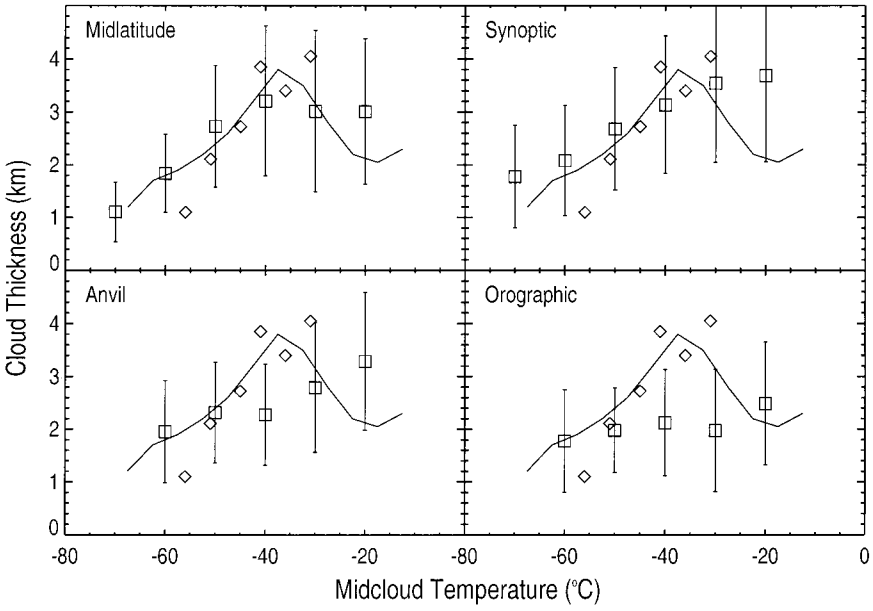

FIG. 5. Relations between Δz and T_m for the four cirrus categories in 10°C T_m intervals (squares with standard deviations). The line shows the Southern Hemisphere midlatitude cirrus relation from Platt and Dilley (1981), and the ◇ are from Minnis et al. (1990).

the lidar return is dominated by single backscattering (with some forward scattering). A relatively thicker cloud with a higher optical depth would be assigned $\eta = 0.8$ because of the increased importance of multiple scattering. Finally, optically thick clouds showing evidence for strong laser attenuation will be more dominated by multiple scattering, and therefore a $\eta = 0.6$ or 0.7 is used.

We determine k by first calculating the average $\beta_c(z)$ between the top of the lidar signal and a height just above the cloud top $\overline{\beta}_c(z_t, z_{\text{top}})$ using various values of the parameter $k/2\eta$ over a range of k from 0.01 to 0.2 sr^{-1}. The slope of the curve that relates $k/2\eta$ and $\overline{\beta}_c(z_t, z_{\text{top}})$ is also calculated. As the change in slope becomes small, the change in $\beta_c(z)$ associated with changes in k diminish. The point where this occurs is where the solution to $k/2\eta$ is determined. If this value is too low, the solution will be unstable, if it is too large, τ will be underestimated (see Barnett 2000). Once $k/2\eta$ is estimated, η is used to determine k, and τ is calculated by integrating $\beta_c(z)$ between the cloud base z_b and cloud top z_t using the equation

$$\tau = \frac{1}{k}\int_{z_b}^{z_t} \beta_c(z)\, dz. \tag{3}$$

The overall uncertainty in estimating τ, including the uncertainty in choosing a value for η, is ~30%. Although this number seems high, it is well within the required uncertainty needed for climate studies (Brown et al. 1995).

In order to calculate the cloud emittance, the radiance due to the emission of ice crystals in the cloud I_c is estimated by removing the contributions due to gases such as water vapor, carbon dioxide, and ozone from the IR measured radiance I_m following

$$I_c = (I_m - I_{\text{sr}}T_{\text{bc}} - I_g)/T_{\text{bc}}, \tag{4a}$$

where

$$I_g = I_{\text{ac}}T_cT_{\text{bc}} + I_{\text{ic}}T_{\text{bc}} + I_{\text{bc}}. \tag{4b}$$

The transmittance below the cloud T_{bc}, and the radiance due to the emission of atmospheric gases above the cloud I_{ac}, below the cloud I_{bc}, and in the cloud I_{ic} are derived using a correlated k distribution model designed specifically for the bandwidth and filter function of the radiometer (Duffy 1996; Barnett 2000). The I_{sr} represents the upwelling radiance that is reflected off the cloud down into the beam of the radiometer. A diagram depicting the various components of the measured radiance is provided in Fig. 6.

As underscored in Platt (1973), I_{sr} can be an important contributor to I_m. An improved technique for estimating I_{sr} that uses single-scattering properties derived from 28 different ice crystal size distributions obtained during in situ measurements of cirrus clouds (Fu 1996; Fu et al. 1998) has been developed for the FARS LIRAD algorithm. Estimates of cloud reflectance are made using the discrete ordinate algorithm DISORT (Stamnes et al. 1988) at various angles $R(\theta)$ according to the reciprocity principle (Stamnes and Swanson 1981). By estimating the upwelling radiance incident at cloud base $I^{\uparrow}(z_0, \theta)$,

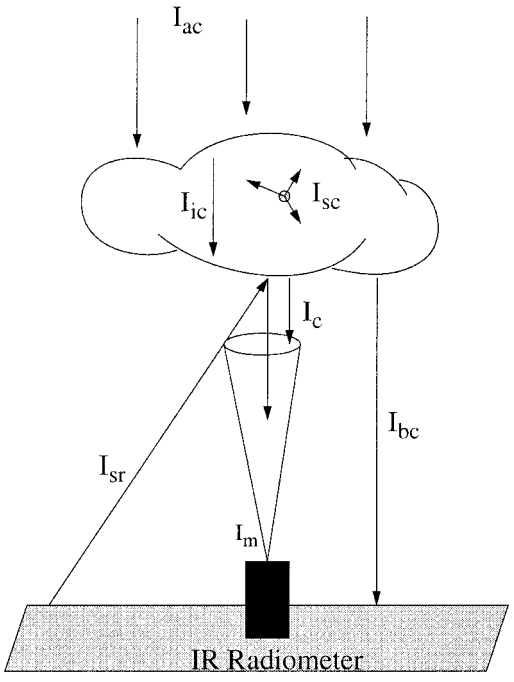

FIG. 6. Schematic rendering of the radiances that are measured by the infrared radiometer used in the LIRAD method. The I_{ac}, I_{ic}, and I_{bc} represent radiances due to the emission of gases, whereas I_c and I_{sc} represent radiant emission from ice crystals within the cirrus cloud.

I_{sr} can be determined by integrating over various angles according to the equation

$$I_{sr} = \frac{1}{4\pi}\int_0^{80^\circ} I^{\uparrow}(z_0, \theta)R(\theta)\, d\theta. \tag{5}$$

Calculations of I_{sr} for each size distribution and various values of τ have revealed three distinct size categories based on the generalized effective size as defined by Fu (1996). The single-scattering properties are chosen based on these size categories and information concerning the observed cloud type as revealed by lidar measurements and field notes. For example, the appearance of atmospheric optical phenomena such as coronas or aureola are associated with small particles (Sassen 1997), in which case the single-scattering properties for a small size distribution is used. The presence of oriented hexagonal plates, which can be identified using the linear depolarization ratio (see Part II), and other crystals often associated with the presence of halos, usually have larger sizes. The choice of size distribution used to calculate I_{sr} introduces a $<2\%$ uncertainty in the estimation of ϵ, mainly because the relative contribution of I_{sr} to the measured radiance is small.

Once I_c is determined, the absorption coefficient $\sigma_a(z)$ is calculated as a function of height by assuming there is a relationship between $\beta_c(z)$ and $\sigma_a(z)$ of the form $\sigma_a(z) = \zeta\beta_c(z)$, using an initial guess of ζ (Platt 1973). The theoretical cloud radiance I_{at} is calculated following Platt and Dilley (1981), and ζ is varied until $I_{at} \cong I_c$. The final values of $\sigma_a(z)$ are used to derive the cloud emittance from

$$\varepsilon = 1 - \exp\left(-\int_{z_b}^{z_t} \sigma_a(z)\, dz\right). \tag{6}$$

4. Visible cloud optical depth

Provided in Fig. 7 are the PDFs of τ for the total midlatitude cirrus dataset, and the samples stratified by

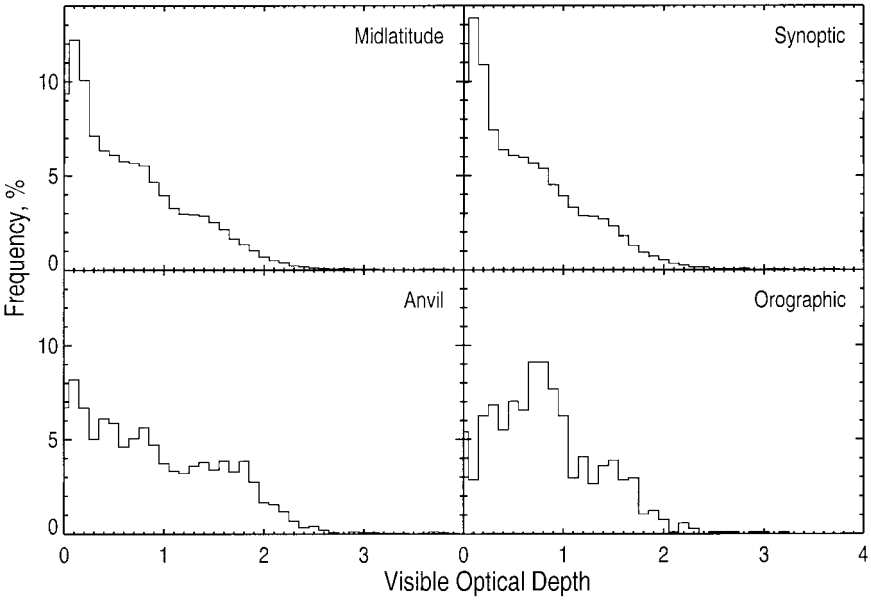

FIG. 7. PDFs of τ for the four cirrus categories.

TABLE 3. Statistics of radiative properties for the combined FARS midlatitude cirrus and each cirrus generating category.

	Mean	Median
	Visible optical depth	
Midlatitude	0.751 ± 0.91	0.609
Synoptic	0.673 ± 0.74	0.534
Anvil	0.946 ± 0.68	0.830
Otographic	0.864 ± 0.53	0.805
	Cloud emittance	
Midlatitude	0.296 ± 0.22	0.245
Synoptic	0.262 ± 0.19	0.217
Anvil	0.365 ± 0.25	0.316
Orographic	0.344 ± 0.21	0.320

generating mechanism. Table 3 gives the mean and standard deviation, and median of τ for these samples. Recalling that subvisual or very thin cirrus with $\tau < \sim 0.05$ are generally absent in this sample, it is clear that the optically thinnest cirrus are the most abundant for all conditions except orographic cirrus. (Orographic cirrus clouds tend to generate higher τ because of their local generation at relatively high updraft velocities, while the anvil category shows a secondary maximum at ~1.5 probably due to much the same reasons.) The frequency of τ values decreases steadily until few cases approach the $\tau \approx 3.0$ limit that lidar (with analog detectors) can measure effectively (Kinne et al. 1992; Sassen and Cho 1992). The mean τ in Table 3 are somewhat under 1.0, but vary with generating mechanism. In Table 4 are shown the percentages for thin (i.e., bluish-appearing) cirrus of $\tau < \sim 0.3$ and for rather opaque cirrus of $\tau >$ 1.0. Although the total cirrus sample has frequencies of ~30% in these two regimes, orographic cirrus rarely appear thin and anvil cirrus are often dense. The ~50% value for $\tau < \sim 0.3$ reported in Part I used a different cirrus sample that included very thin and subvisual cirrus, and τ was merely estimated from the visual appearance of the cirrus near the zenith.

The dependence of τ on Δz is shown in Fig. 8, and on temperature in Fig. 9, for the total midlatitude cirrus sample. (The plots for the anvil and orographic cirrus categories are similar, but display some irregularities attributable to the smaller sample sizes.) It is apparent that τ increases in a linear fashion with increasing Δz and T_m. These basic tendencies are primarily related to the action of the adiabatic process in cirrus clouds, which liberates ice mass during diffusional growth as a strong function of temperature. Note that increasing Δz also tends to increase T_m according to Fig. 5.

TABLE 4. Amount of cirrus observations in percent that fall in certain categories of their radiative properties.

	$\tau < 0.3$	$\tau > 1.0$	$\varepsilon < 0.3$	$\varepsilon > 0.7$
Midlatitude	30.3	28.7	58.2	5.01
Synoptic	34.2	24.5	63.8	1.81
Anvil	21.6	41.5	47.9	11.8
Orographic	14.5	33.7	45.5	5.21

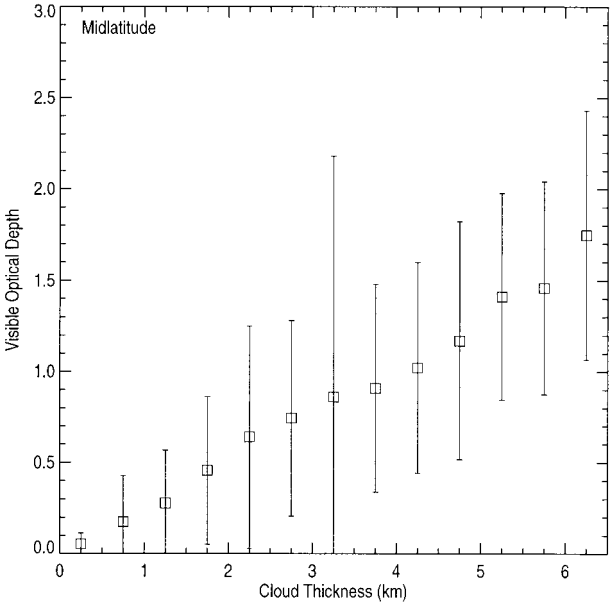

FIG. 8. Dependence of τ on 0.5-km intervals of Δz for the midlatitude cirrus sample, shown with standard deviations.

5. Infrared layer emittance

As with the case for τ, we begin the analysis of derived ϵ by showing in Fig. 10 the PDFs in 0.05 ϵ intervals for the four cirrus cloud categories, and we provide mean and median values in Table 3, and characteristic values for certain ranges in Table 4. Similar to

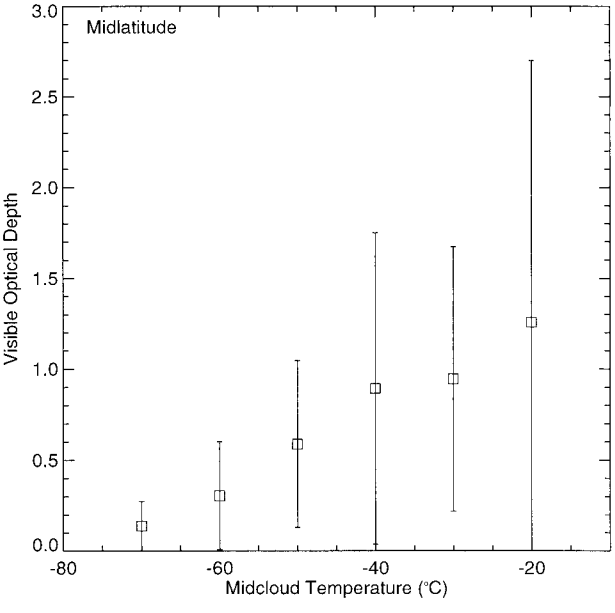

FIG. 9. As in Fig. 8, except for 10°C T_m intervals.

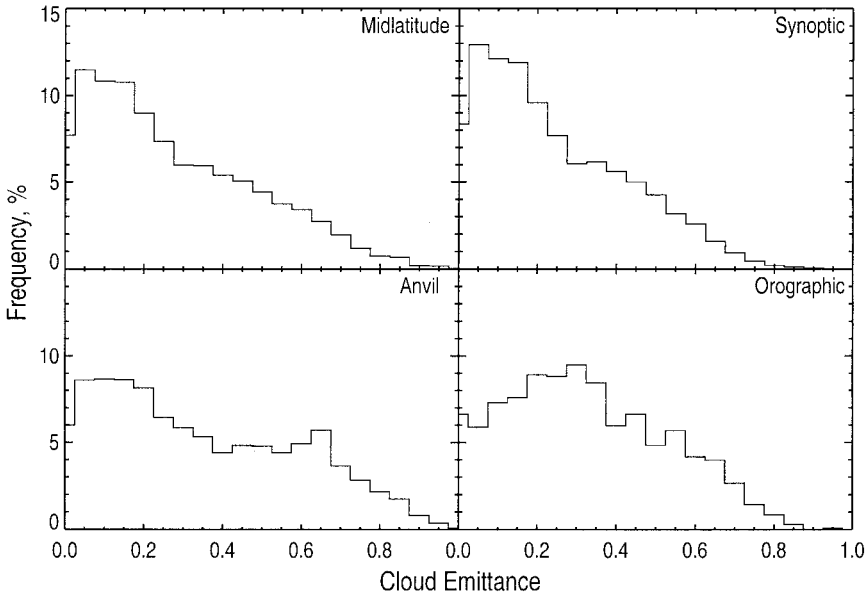

FIG. 10. PDFs of ϵ for the four cirrus categories.

the behavior in the visible portion of the spectrum, the midlatitude and synoptic PDFs show a steady decrease in frequency with increasing ϵ. As noted above, the frequency of the smallest ϵ bin has been reduced by the inherent difficulties of the LIRAD method in dealing with very thin cirrus. In contrast to synoptic cirrus, the orographic cirrus distribution displays a lognormal shape with a median of ~0.3, and anvil cirrus display a bimodal pattern, which may be due to sampling both local developing anvils and more aged anvil remnants. The data in Table 3 reveal that anvil and orographic cirrus have the highest mean and median ϵ, as is also the case for τ. The greater activity in the infrared of these cloud types is evident in Table 4, where anvil cirrus clouds have a much higher frequency of $\epsilon > 0.7$.

Figure 11 depicts the dependence of ϵ on T_m for the total and each cirrus category. Our midlatitude findings are compared with results from Southern Hemisphere (Platt and Dilley 1981) and equatorial (Platt et al. 1998) cirrus. Although our findings are in reasonable compli-

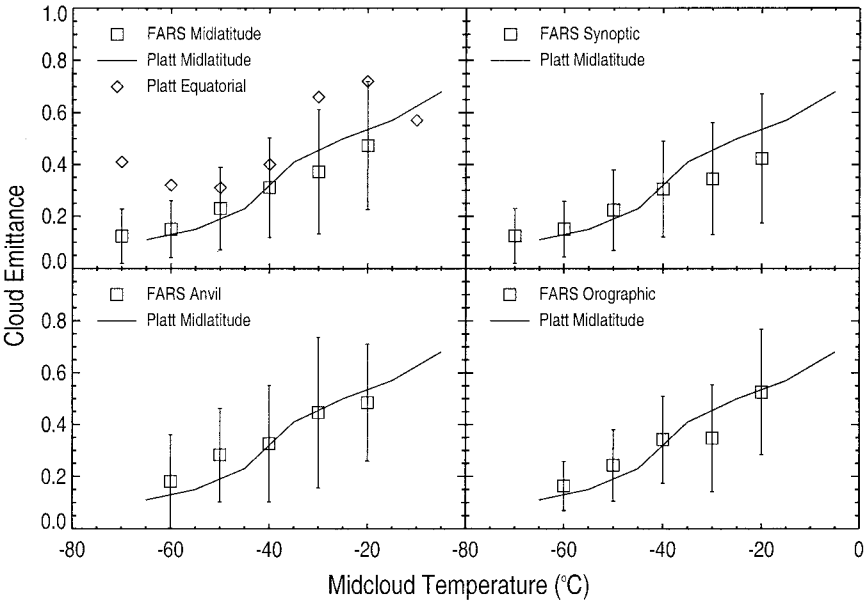

FIG. 11. Dependence of ϵ on T_m (squares with standard deviations), compared with Southern Hemisphere midlatitude (line; from Platt and Dilley 1981) and equatorial (◇; from Platt et al. 1998) cirrus.

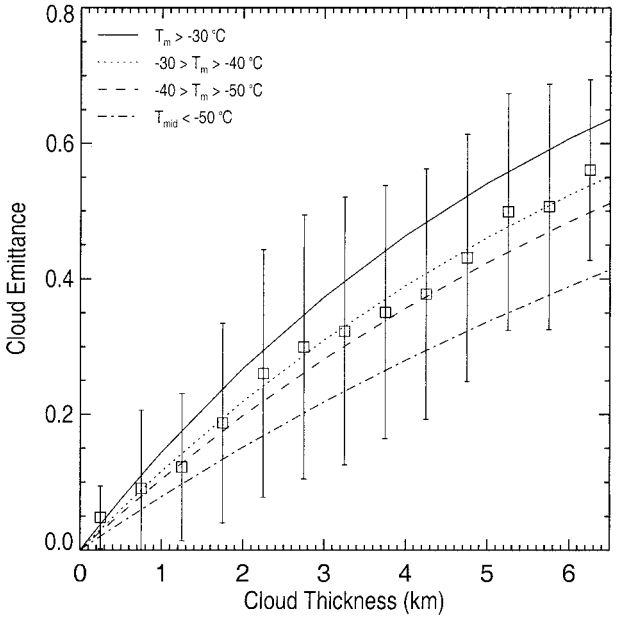

FIG. 12. Dependence of ϵ on Δz for the midlatitude cirrus in terms of average values over 0.5-km Δz intervals (squares with standard deviations), and fitted curves over the indicated T_m ranges.

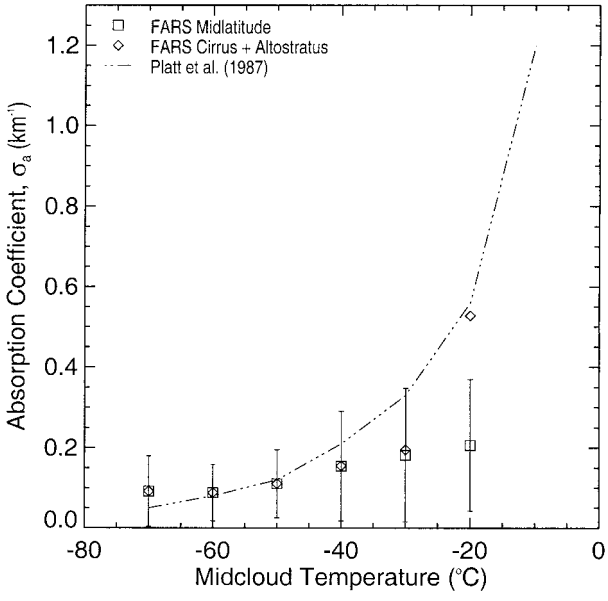

FIG. 13. Average infrared absorption coefficients in 10°C T_m intervals for midlatitude cirrus, with standard deviations, compared with Southern Hemisphere midlatitude cirrus (line; from Platt et al. 1987), and showing the effect of including altostratus cloud measurements in the FARS cirrus sample (diamonds).

ance with the Australian midlatitude data, they differ from the tropical trend, which is based on a short (12 day) period of cirrus observations. All FARS cirrus cloud categories show a similar trend of increasing ϵ with warming temperatures. As far as the dependence on Δz for midlatitude cirrus is concerned, a gradual increase in ϵ with Δz is shown in Fig. 12 in terms of the mean (with standard deviations) and parameterized results (see below) that divide the data into the indicated T_m intervals. Here, a clear temperature dependence is depicted.

6. Backscattering parameters

In addition to the vertically integrated ϵ and τ data quantities, other parameters of importance to radiative transfer and lidar research can be evaluated on the basis of the FARS cirrus dataset. In Fig. 13 are given the dependence of the 9.5–12.0-μm absorption coefficient σ_a on T_m for the midlatitude cirrus. The positive correlation between absorption and temperature to be expected from the action of the adiabatic process is clearly evident. However, the agreement of σ_a with previous research from southern Australia (Platt et al. 1987) is only reasonable for the coldest T_m. Note that the ♢ symbols in Fig. 13 depict the effect of including altostratus cloud data into our midlatitude sample. Given the warm (−10°C) T_m data treated by Platt et al. (1987), which violates our criteria for cirrus clouds (Sassen 2001; Part I), the differences in the curves can be accounted for by assuming that their sample included some midlevel clouds.

There is also poor agreement in the average temperature dependence of α, the ratio of the layer-integrated σ_e and σ_a coefficients (Fig. 14). A value of $\alpha = 2.0$ represents the ''large-particle'' geometrical optics limit, which our results approach at warm cirrus temperatures. The larger ~3.0 value at −70°C indicates that at these frigid temperatures the mean particle size is small

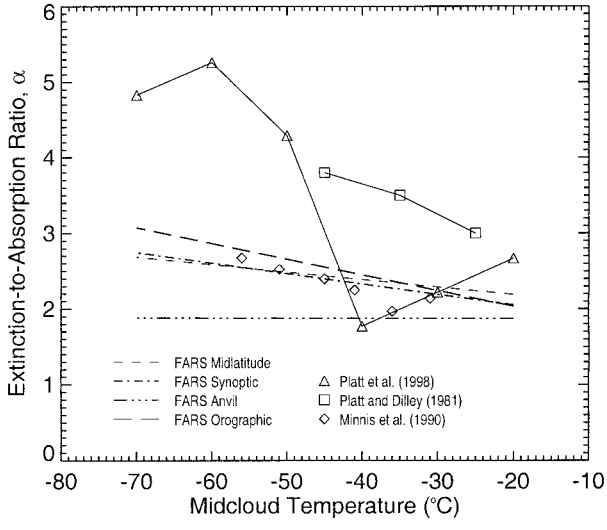

FIG. 14. Visible extinction to infrared absorption coefficient ratios plotted as a function of T_m for the four FARS cirrus categories, compared with data from equatorial (Platt et al. 1998), Southern Hemisphere (Platt and Dilley 1981), and FIRE IFO (Minnis et al. 1990) midlatitude cirrus.

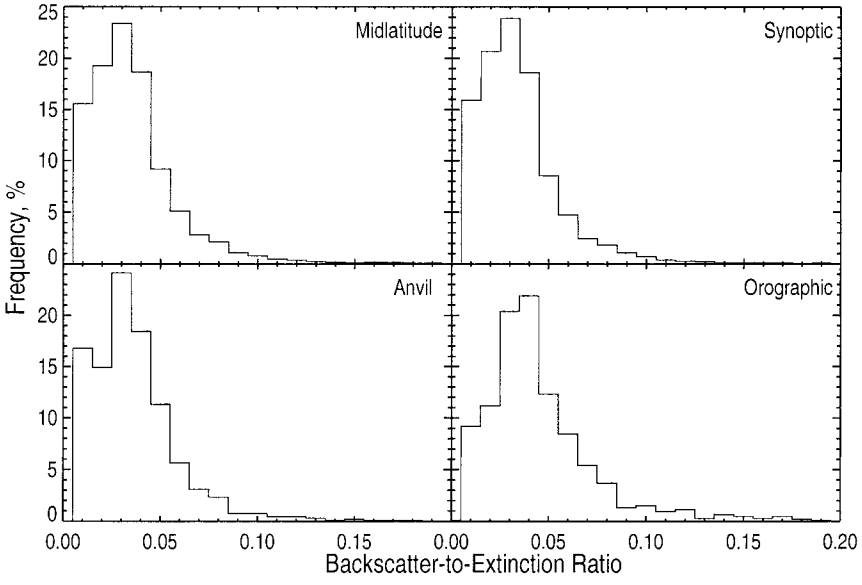

FIG. 15. PDFs of the backscatter-to-extinction ratio k for the four cirrus categories.

enough, especially for orographic cirrus of local (i.e., recent) origin, to cause σ_a to shift from area- to volume-dependent absorption (Mitchell et al. 1996). Anvil cirrus, on the other hand, display a flat curve indicating little temperature-versus-particle size effects; that is, the particles are uniformly large. Although often being newly formed, anvil cirrus composition may be dominated by the effects of strong convective updrafts, which introduce large ice particles formed at lower levels. The results for Southern Hemisphere and equatorial cirrus are noticeably different, and would imply the dominance of the effects of minute micron-sized particles. Added to Fig. 14 are the α derived in Minnis et al. (1990) from combined lidar and satellite radiance data, similar to the LIRAD approach. These points are derived from the average 1986 FIRE IFO and case study data, and lie close to our curves fitted to scatterplots of individually calculated α versus T_m.

The backscatter-to-extinction ratio k is an important parameter for lidar remote sensing, and greater knowledge of its variability in cirrus clouds would be of benefit to simple (i.e., non-Raman or -high spectral resolution) lidar systems that do not directly measure this quantity. Although our approach in estimating k neglects the extra multiple scattering β' term in Eq. (1) (in contrast to the problem of treating this effect in the exponential extinction term, which may yield the impossible but expedient $\eta < 0.5$), our method for estimating η based on cirrus height and thickness should yield reasonable values. The result of our analysis, which is inherent in the derivation of τ, is given in Fig. 15, with mean and median k values compiled in Table 5. The fact that k peaks at higher values for orographic cirrus may reflect the microphysical implications for the radiative properties of newly formed cirrus undergoing rapid cooling. Both experiments (Sassen 1978) and theory (Takano and Liou 1995) have indicated that k is controlled by the complexity of ice particle shape and aspect ratio. Note also that the presence of the ''tails'' of high k in Fig. 15 result from another scattering process: the anisotropic effect of cirrus containing horizontally oriented planar ice crystals (Part II), which can considerably increase k by virtue of the unusually strong backscattering measured by a zenith lidar.

These k values are consistent with a number of previous studies of cirrus with peak frequencies generally in the range of ~0.02–0.04 sr^{-1} (Grund and Eloranta 1990; Sassen and Cho 1992; Eloranta et al. 1998; Sauvage et al. 1999). Finally, the relation between k and τ is shown in Fig. 16. There is a tendency for k to increase at large τ, which may reflect of the effects of changes in ice particle shape and size with temperature (Part II), as well as potential problems with treating multiple backscattering in dense cirrus using a 1.0 mrad FOV lidar.

TABLE 5. Statistics for the lidar backscatter-to-extinction ratio k (sr^{-1}) for all cirrus and each cloud generating mechanism.

	Mean	Median
Midlatitude	0.041 ± 0.026	0.037
Synoptic	0.039 ± 0.025	0.035
Anvil	0.041 ± 0.023	0.038
Orographic	0.050 ± 0.028	0.044

7. Parameterizations

The basic temperature dependence in the radiative properties of cirrus clouds revealed in the extensive FARS dataset (Figs. 8, 9, 11, 13, and 14) is a conse-

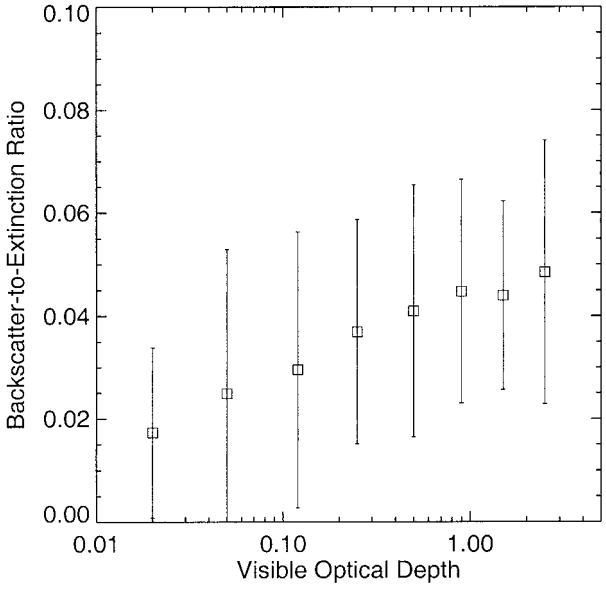

FIG. 16. Dependence of the backscatter-to-extinction ratio k on τ for our midlatitude cirrus sample, with standard deviations.

quence of the adiabatic process, which liberates condensate as a strong function of temperature. Hence, a basic temperature dependence of ice water content and effective particle size is built into the adiabatic ascent of saturated air, although a particular cloud volume may not have true adiabatic content because of a number of cloud processes. These processes include mixing with dry air along cloud boundaries, and the transport of particles by turbulence, gravitational sedimentation, and vertical air velocities, which all lead to local variations in ice water content and the shape of the particle size distribution (Khvorostyanov and Sassen 1998). As a consequence, both models and in situ measurements (e.g., Sassen et al. 1989) show a characteristic vertical structure to cirrus clouds: a near cloud top generating region containing small ice crystals nucleated at relatively high ice supersaturations, an ice-saturated growth region throughout most of the depth of the cloud, and finally a subsaturated evaporation region near cloud base. Thus, it should be remembered that ϵ and τ are quantities that are integrated vertically through characteristically inhomogeneous clouds.

The fitted curves in Fig. 12 provide the basis for our argument that both Δz (km) and T_m (°C), two variables commonly predicted in large-scale models, must be included in any parameterization of optical properties. It is clear that the relation between ϵ and Δz is a strong function of T_m. Our parameterization of cirrus ϵ and τ begins with the mean cloud layer σ_a (km^{-1}) from LIRAD-derived ϵ via the relation

$$\epsilon = 1 - \exp(-\sigma_a \Delta z), \tag{7}$$

where $\sigma_a \Delta z$ is the absorption optical depth. An empirical

TABLE 6. Numerical coefficients for Eqs. (8), (9), and (10) derived for all cirrus observations and the primary generating mechanisms. Numbers in parentheses denote the uncertainty in each coefficient.

	A	A'	B
Midlatitude	8.5×10^{-5}	1.57×10^{-4}	0.51
	(1.4×10^{-6})	(6.1×10^{-8})	(1.9×10^{-3})
Synoptic	7.6×10^{-5}	1.47×10^{-4}	0.50
	(1.5×10^{-8})	(2.3×10^{-6})	(6.9×10^{-3})
Anvil	9.9×10^{-5}	1.72×10^{-4}	0.55
	(3.5×10^{-6})	(4.1×10^{-6})	(1.7×10^{-2})
Orographic	1.3×10^{-4}	2.13×10^{-4}	0.55
	(7.7×10^{-6})	(9.0×10^{-7})	(2.8×10^{-2})

relation of the form proposed by Platt and Harshvardhan (1988, hereafter PH88),

$$\sigma_a = A(T_m + 80°\text{C})^2, \tag{8}$$

is then derived after performing a numerical fit to a scatterplot of (24 289) σ_a versus T_m. Similarly, the mean cloud layer σ_e may be parameterized as

$$\sigma_e = A'(T_m + 80°\text{C})^2, \tag{9}$$

where $\sigma_e = \tau/\Delta z$. Values for the coefficients A and A' are given in Table 6, which also provides the uncertainties derived from curve fitting the dataset as represented by their standard deviations. This shows that the uncertainties in the coefficients are small, such that the numerical fit provides a good representation of the relationship between the two variables.

In Fig. 17 we compare the PH88 parameterization with our results stratified by our main cirrus categories. The curves for the midlatitude cirrus and other varieties are clearly different from the PH88 curve, although the

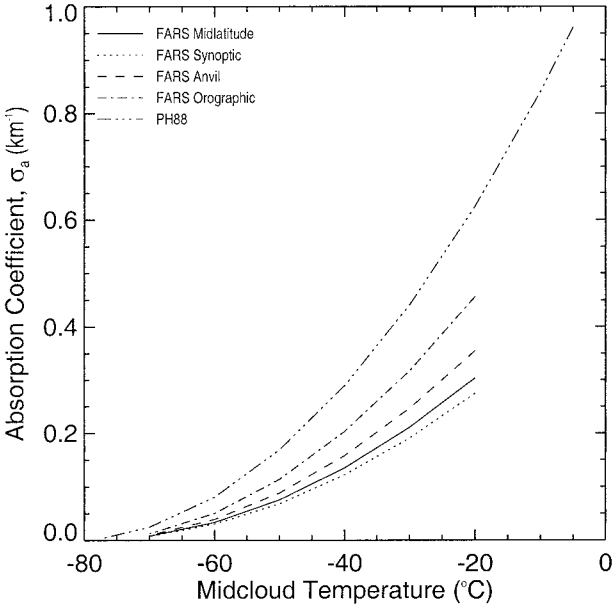

FIG. 17. Comparison of parameterized infrared absorption coefficients vs T_m for our cirrus categories and that of Platt and Harshvardhan (1988; PH88) over the valid T_m ranges.

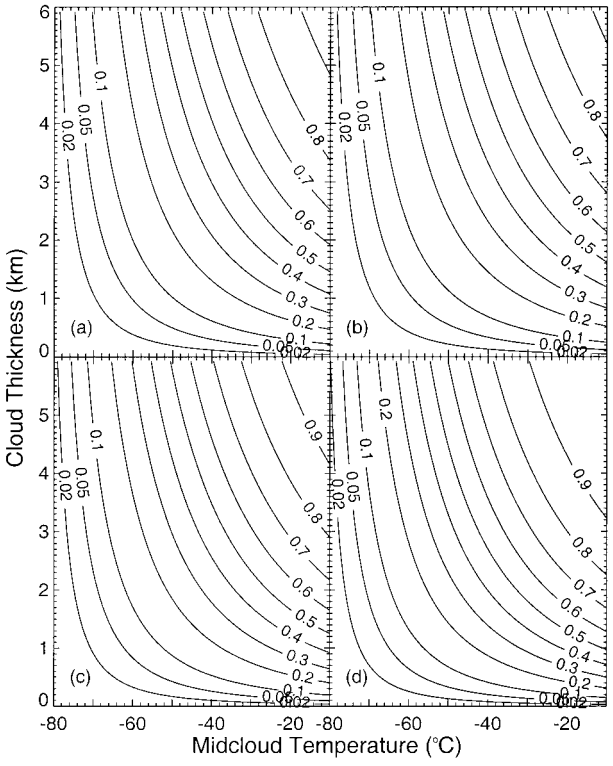

FIG. 18. Contours of ϵ showing the parameterized relationships between Δz and T_m for (a) midlatitude, (b) synoptic, (c) anvil, and (d) orographic cirrus.

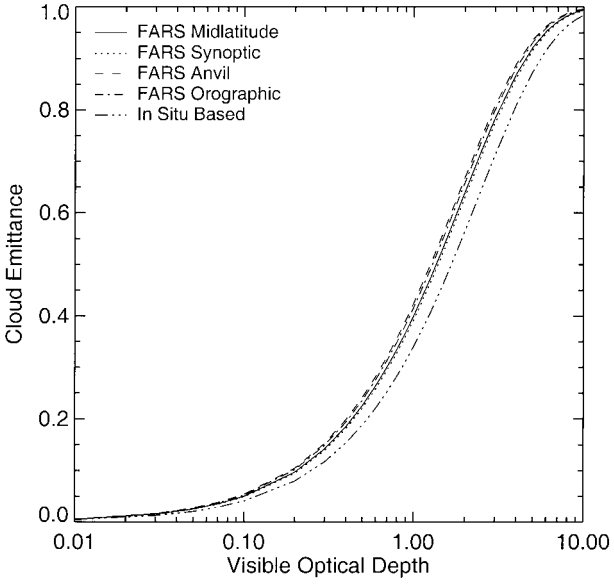

FIG. 19. Comparison of parameterizations relating τ to ϵ for our cirrus categories with the result calculated from in situ size spectra data.

orographic relation comes closest. As discussed earlier, this is likely a consequence of including middle-level clouds in the PH88 results, which although only influencing the data at the warmest T_m, still has an effect on curve fitting.

By inserting Eq. (8) into Eq. (7), ϵ can be estimated using only Δz and T_m as variables. The results of this parameterization are shown in Fig. 18 for the various cirrus categories, providing the fields of ϵ (solid lines) as functions of these variables. A strong effect of temperature on ϵ is once again evident.

Lastly, ϵ is related to τ through the use of the empirical relationship

$$\epsilon = 1 - \exp(-B\tau), \tag{10}$$

where Table 6 also lists the numerical coefficients B. Fu and Liou (1993) offered a similar relation using a radiative parameterization based on in situ ice crystal size distribution measurements. This and other approaches rely on an exponential ϵ versus τ relationship, which is verified by our extensive remote sensing results. More recent results suggest a value of $B = 0.42$ (Q. Fu 1999, personal communication). As shown in Fig. 19, the agreement with this new parameterization is quite good despite the different approaches used. Finally, note that a comparison of our midlatitude cirrus parameterization with those for midlevel (altocumulus and altostratus) clouds have recently been given in Sassen et al. (2001b) in an attempt to achieve a broader understanding of cloud radiative effects.

8. Conclusions

This study is based on an extensive 7-yr program of coaligned polarization lidar and midinfrared radiometer measurements of cirrus clouds identified in each case by visual inspection. Our program at FARS, currently in its 12th year, has been intended for basic high-cloud research and to support the satellite cloud algorithm validation effort of FIRE. As illustrated here and in Parts I and II, this ground-based remote sensing program represents a unique resource for improving our knowledge of the impact of clouds on climate. This dataset has yielded a climatologically significant database of midlatitude cirrus cloud radiative and laser backscattering properties, which, however, will be to some extent specific to our midlatitude location (see Part I).

Our findings based on a new LIRAD approach reaffirm the quintessential optical property of cirrus clouds, their optical *thinness* relative to other clouds. Although the LIRAD method has difficulties with the thinnest and thickest cirrus clouds, our derived values of τ range from $\sim$0.003 to 3.0, and of ϵ from $\sim$0 to 0.85. About 30% of cirrus have $\tau < 0.3$ (Table 4), which approximately corresponds to thin (semitransparent) cirrus. For the entire FARS cirrus sample, the mean and median values are 0.75 ± 0.91 and 0.61 for τ, and 0.30 ± 0.22 and 0.25 for ϵ. These findings have obvious implications for assessing the efficacy of satellite methods for detecting and identifying midlatitude cirrus from

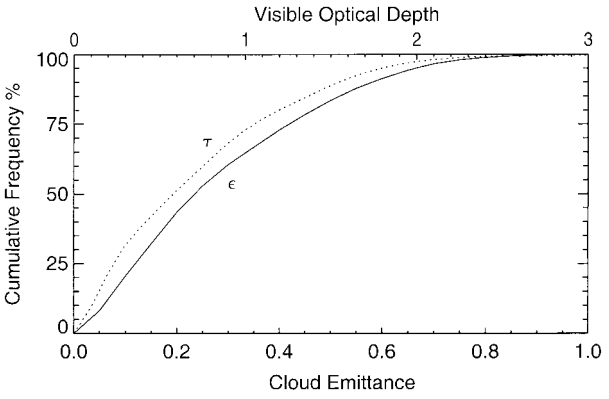

FIG. 20. Cumulative frequency distributions for ϵ (solid) and τ from the midlatitude cirrus sample.

upwelling radiance data. Thus we provide in Fig. 20 the cumulative frequency distributions for ϵ and τ, from which the percentage of our midlatitude cirrus clouds that are detectable by satellite-based or other instruments with known thresholds can be estimated.

Comparison with other midlatitude research reveals areas of agreement, but also some significant discrepancies that may be related to the assumptions made in the LIRAD method, the composition of the cirrus cloud samples, and geographical differences in cirrus types. The average relation between ϵ and T_m (Fig. 11) for Northern and Southern Hemisphere midlatitude cirrus is similar, and in compliance with data obtained from FIRE IFO cirrus using combined lidar and satellite information. However, the limited evidence thus far available from equatorial cirrus implies that they may be distinct from both midlatitude anvil and synoptic cirrus. We conclude that further research into cumulonimbus-derived tropical cirrus is needed so more reliable parameterizations can be made.

The agreement of our parameterized ϵ versus τ relation (Fig. 19) with theoretical predictions based on in situ measured cirrus particle size distributions is very good considering the dissimilar approaches used, suggesting that this radiative problem is well understood. However, we find that the PH88 parameterization of σ_a versus T_m differs significantly from our results, unless we include the contributions from altostratus clouds at the warmest temperatures in our cirrus domain. The inclusion of thick ice clouds in a cirrus sample may, in particular, cause problems because of ''warm'' (~ -15°C) ice crystal aggregation effects on cloud radiative properties. This suggests that the larger FARS dataset is more representative of midlatitude cirrus because of our reliance on visual cloud identification. The parameterizations we have developed should provide for the improved numerical treatment of the radiative effects of cirrus clouds.

It has also been possible, due to our large dataset, to examine for the first time the differences in radiative properties attributable to some of the primary cirrus cloud generation mechanisms (Sassen 2001). These effects are rooted in fundamental cirrus cloud microphysical processes that control cloud composition as functions of temperature and updraft velocity. Moreover, implicit in our cirrus categories is a measure of the *age* of the cloud: whereas long-lived synoptic cirrus are typically in a regenerative maintenance stage, local orographic and anvil cirrus are young and still developing. All these variables affect the cirrus cloud particle shape, concentration, growth rate, fall speed, and size distribution, which in combination modulate their radiative effects.

Although the largest difference from midlatitude synoptic cirrus cloud properties is associated with local orographic cirrus having relatively large updraft velocities and warm temperatures, these clouds probably represent only a minor contributor to cirrus globally. Anvils, on the other hand, may be seasonally/regionally abundant sources of cirrus, and are likewise indicated to have somewhat distinct optical properties as a result of the strong convective updrafts and the introduction of boundary layer aerosols into the relatively clean upper troposphere. Consequences of anvil cirrus having greater ϵ may include higher ice mass contents and higher albedos, which has recently been indicated by Heymsfield and McFarquhar (1996). Such considerations introduce a new aspect into improving the treatment of the global varieties of cirrus clouds in large-scale models, and retrieving their properties from satellites.

Acknowledgments. Recent funding has come from NSF grant ATM-9528287 and NASA Grant NAC-2-1106 for FARS research, and DOE Grant DEFG0394ER61747 from the Atmospheric Radiation Measurement program for parameterization development. We thank the reviewers for their comments.

REFERENCES

Barnett, J. M., 2000: Remote sensing of midlatitude cirrus radiative properties: A seven-year climatology. Ph.D. thesis, University of Utah, 220 pp.

Brown, P. R. A., A. J. Illingworth, G. M. MCFarquhar, K. A. Browning, and M. Gosset, 1995: The role of spaceborne millimeter-wave radar in the global monitoring of ice cloud. *J. Appl. Meteor.*, **34,** 2346–2366.

Comstock, J. M., and K. Sassen, 2001: Retrieval of cirrus cloud radiative and backscattering properties using combined lidar and infrared radiometer (LIRAD) measurements. *J. Atmos. Oceanic Technol.*, in press.

Cox, S. K., D. S. McDougal, D. A. Randall, and R. A. Schiffer, 1987: FIRE—The First ISCCP Regional Experiment. *Bull. Amer. Meteor. Soc.*, **68,** 114–118.

Duffy, K. J., 1996: A radiative transfer model to analyze radiometer data in the atmospheric window. M.S. thesis, University of Utah, 94 pp.

Eloranta, E. W., R. E. Kuehn, and R. E. Holz, 1998: Measurements of backscatter phase function and depolarization in cirrus clouds made with the University of Wisconsin High Spectral Resolution Lidar. *4th Int. Symp. on Tropospheric Profiling,* Snowmass, CO.

Fu, Q., 1996: An accurate parameterization of the solar radiative

properties of cirrus clouds for climate models. *J. Climate,* **9,** 2058–2082.
——, and K.-N. Liou, 1993: Parameterization of the radiative properties of clouds. *J. Atmos. Sci.,* **50,** 2008–2025.
——, Y. Ping, and W. B. Sun, 1998: An accurate parameterization of the infrared radiative properties of cirrus clouds for climate models. *J. Climate,* **11,** 2223–2237.
Grund, C. J., and E. W. Eloranta, 1990: The 27–28 October 1986 FIRE IFO cirrus case study: Cloud optical properties determined by High Spectral Resolution Lidar. *Mon. Wea. Rev.,* **118,** 2344–2355.
Heymsfield, A. J., and G. M. McFarquhar, 1996: High albedos of cirrus in the tropical Pacific warm pool: Microphysical interpretations from CEPEX and from Kwajalein, Marshall Islands. *J. Atmos. Sci.,* **53,** 2424–2451.
Khvorostyanov, V. I., and K. Sassen, 1998: Cirrus cloud simulation using explicit microphysics and radiation. Part II: Microphysics, vapor and mass budgets, and optical and radiative properties. *J. Atmos. Sci.,* **55,** 1822–1845.
Kinne, S., T. P. Ackerman, A. J. Heymsfield, F. P. J. Valero, K. Sassen, and J. D. Spinhirne, 1992: Cirrus microphysics and radiative transfer: Cloud field study on 28 October 1986. *Mon. Wea. Rev.,* **120,** 661–684.
Liou, K.-N., 1986: The influence of cirrus on weather and climate processes: A global perspective. *Mon. Wea. Rev.,* **114,** 1167–1199.
Minnis, P., D. F. Young, K. Sassen, J. M. Alvarez, and C. J. Grund, 1990: The 27–28 October 1986 FIRE IFO cirrus case study: Cirrus parameter relationships derived from satellite and lidar data. *Mon. Wea. Rev.,* **118,** 2402–2425.
Mischenko, M. L., J. W. Hovenier, and L. D. Travis, Eds., 2000: *Light Scattering by Nonspherical Particles: Theory, Measurements, and Geophysical Applications.* Academic Press, 690 pp.
Mitchell, D. L., A. Macke, and Y. Liu, 1996: Modeling cirrus clouds. Part II: Treatment of radiative properties. *J. Atmos. Sci.,* **53,** 2967–2988.
Ou, S.-C., and K.-N. Liou, 1995: Ice microphysics and climatic temperature feedback. *Atmos. Res.,* **35,** 127–138.
Platt, C. M. R., 1973: Lidar and radiometric observations of cirrus clouds. *J. Atmos. Sci.,* **30,** 1191–1204.
——, and A. C. Dilley, 1981: Remote sensing of high clouds, Part IV, Optical properties of midlatitude and tropical cirrus. *J. Atmos. Sci.,* **38,** 1069–1082.
——, and Harshvardhan, 1988: Temperature dependence of cirrus extinction: implications for climate feedback. *J. Geophys. Res.,* **93,** 11 051–11 058.
——, J. C. Scott, and A. C. Dilley, 1987: Remote sounding of high clouds. Part VI: Optical properties of midlatitude and tropical cirrus. *J. Atmos. Sci.,* **44,** 729–747.
——, S. A. Young, P. J. Manson, G. R. Patterson, S. C. Marsden, R. T. Austin, and J. H. Churnside, 1998: The optical properties of equatorial cirrus from observations in the ARM Pilot Radiation Observation Experiment. *J. Atmos. Sci.,* **55,** 1977–1996.
Sassen, K., 1978: Backscattering cross sections for hydrometeors: Measurements at 6328 Angstroms. *Appl. Opt.,* **17,** 804–806.
——, 1997: Contrail-cirrus and their potential for regional climate change. *Bull. Amer. Meteor. Soc.,* **78,** 1885–1903.
——, 2001: Cirrus clouds: A modern perspective. *Cirrus,* D. Lynch et al., Eds., Oxford University Press, 11–40.
——, and B. S. Cho, 1992: Subvisual-thin cirrus lidar dataset for satellite verification and climatological research. *J. Appl. Meteor.,* **31,** 1275–1285.
——, and H. Zhao, 1995: Lidar multiple scattering in water droplet clouds: Toward an improved treatment. *Opt. Rev.,* **2,** 394–400.
——, and S. Benson, 2001: A midlatitude cirrus cloud climatology from the Facility for Atmospheric Remote Sensing. Part II: Microphysical properties derived from lidar depolarization. *J. Atmos. Sci.,* **58,** 2103–2112.
——, and J. R. Campbell, 2001: A midlatitude cirrus cloud climatology from the Facility for Atmospheric Remote Sensing. Part I: Macrophysical and synoptic properties. *J. Atmos. Sci.,* **58,** 481–496.
——, D. O'C. Starr, and T. Uttal, 1989: Mesoscale and microscale structure of cirrus clouds: Three case studies. *J. Atmos. Sci.,* **46,** 371–396.
——, J. M. Comstock, Z. Wang, and G. G. Mace, 2001a: Cloud and aerosol research capabilities at FARS: The Facility for Atmospheric Remote Sensing. *Bull. Amer. Meteor. Soc.,* **82,** 1119–1138.
——, ——, and ——, 2001b: Parameterization of the radiative properties of midlatitude high and middle level clouds. *Geophys. Res. Lett.,* **28,** 729–732.
Sauvage, L. H., H. Chepfer, V. Trouillet, P. H. Flamant, G. Brogniez, J. Pelon, and F. Albers, 1999: Remote sensing of cirrus radiative parameters during EUCREX'94. Case study of 17 April 1995. *Mon. Wea. Rev.,* **127,** 486–503.
Stamnes, K., and R. A. Swanson, 1981: A new look at the discrete ordinate method for radiative transfer calculations in anisotropically scattering atmospheres. *J. Atmos. Sci.,* **38,** 387–399.
——, S. C. Tsay, W. Wiscombe, and K. Jayaweera, 1988: Numerically stable algorithm for discrete-ordinate-method radiative transfer in multiple scattering and emitting layered media. *Appl. Opt.,* **27,** 2502–2509.
Stephens, G. L., S. Tsay, P. W. Stackhouse Jr. and P. J. Flatau, 1990: The relevance of the microphysical and radiative properties of cirrus clouds to climate and climate feedback. *J. Atmos. Sci.,* **47,** 1742–1753.
Takano, Y., and K.-N. Liou, 1995: Solar radiative transfer in cirrus clouds. Part III: Light scattering by irregular ice crystals. *J. Atmos. Sci.,* **52,** 818–837.